

## Research Article

# Elastic-Plastic Behavior of Compacted Loess under Direct and Cyclic Tension

Shixin He and Haibo Bai 

*State Key Laboratory for Geomechanics and Deep Underground Engineering, China University of Mining and Technology, Xuzhou 221008, China*

Correspondence should be addressed to Haibo Bai; bai\_hb@126.com

Received 19 June 2019; Revised 14 August 2019; Accepted 6 September 2019; Published 26 September 2019

Academic Editor: Zhiping Luo

Copyright © 2019 Shixin He and Haibo Bai. This is an open access article distributed under the Creative Commons Attribution License, which permits unrestricted use, distribution, and reproduction in any medium, provided the original work is properly cited.

Tensile strain is one of the main variables that affect fracturing in soil. This paper focuses on an experimental investigation of the deformation characteristics of remolded loess in direct and cyclic tension tests. The material behavior was approximated as elastic-plastic by ignoring the effect of time. In direct tests, the results showed that the change in slope of the stress-strain curve depended on the water content. The plastic constitutive relation was described by two methods. In cyclic loading and unloading tests, the remolded loess exhibited hysteresis (a phase lag), which led to dissipation of the mechanical energy. And no compaction limit phenomenon was found. A simple mathematical model was proposed to predict the plastic cyclic characteristics, and it was validated by the new test data.

## 1. Introduction

In many areas of geotechnical engineering, soil is subjected to tensile stress. Tensile cracks often form in tensile stress regions [1, 2]. Cracks are caused by several factors, such as extrusion, uneven settlement, and dehydration [3–5]. These tensile regions can have negative impacts on infrastructures, such as embankment cracks, slope collapse, and earth-retaining wall instability and so on [6–9]. The wide occurrence of tensile phenomena requires a better understanding of their mechanical properties.

Considerable attention has been focused on the tensile fracturing of soils in recent years, mainly including experimental strength tests [10–14] and strength prediction models [15–18]. As is known, strength and ultimate deformation are two important parameters affecting soil fracture. In previous studies, strength and stress were the main research contents. However, deformation characteristics in tension have been ignored. The usual investigation was just to obtain a full stress-strain curve. Obviously, it is not enough for the study of deformation mechanism.

The tensile deformation increases gradually in the tension region; in addition to the monotonous increasing load, there is also the effect of cyclic load. For example, the temporary earthwork stack around an excavation may accelerate crack expansion in the stretched zone. In underground coal mining, the periodic work on the working face indirectly subject the stretched zone to cyclic loading, which can even cause cracks at the earth's surface. Therefore, it is imperative to conduct investigations of the deformation of soils under direct and cyclic loading.

There are extensive loess areas in western China. Loess are typically a kind of clayey silt, and the silt content (0.005–0.05 mm) is generally greater than 50%. Intact loess features a random particle arrangement, high porosity, and significant number of macropores [19, 20]. Land instability hazards here are common and varied, in which ground fissures and surface subsidence are closely related to tensile characteristics [21]. These disasters have seriously affected the local civil engineering construction and the residents' lives and property. Taking loess as the research object, this paper focuses on an experimental investigation of tensile deformation especially plastic strain as it is thought that the

plastic deformation would play a more disadvantageous role than elastic deformation.

A series of tests was performed on samples with different dry densities and water contents. First, in direct tests, the modulus of elasticity, yield limit, and hardening conditions were obtained and analyzed. Then, the hysteresis loops, dynamic strength, and cyclic plastic strain were discussed in the loading-unloading tests. Eventually, an elastic-plastic phenomenological model was presented to describe the plastic cyclic behaviour of soils. This paper may open up a new realm for soil tension research. The results supplemented the shortcomings of tension deformation. It will provide the reference for fracture-resistant designs, also the evaluation for the safety (stability) of geotechnical construction.

## 2. Test Apparatus

The laboratory tests were carried out with a uniaxial direct tension test apparatus, as illustrated in Figure 1. The apparatus consisted of three systems: load application system, displacement measurement system, and platen regulating system. The rectangular specimen was placed on a platform with uniformly distributed roller bearings on the bottom. The tensile mold comprised two rectangular grooves with sides that were free to open. This design prevented the ends of the specimens from being extruded using clamps. One mold was affixed to the apparatus, and the other was connected to the loading system and could move horizontally. The load application system included a traction rope and weights with capacities of 20 kg. The displacement data were collected by economical and practical dial gauges.

Fifteen grams of epoxy structural adhesive were applied to connect the mold to the specimen before the experiment. There was nearly no stress concentration on the specimen ends to ensure force uniformity over the entire length of the sample. In most tests, the specimen broke into two pieces in the middle (30–90 mm). A detailed description of the tensile equipment was given in our previous paper [22]. The compaction device for the remolded sample is shown in Figure 2. The apparatus contained three components: a hollow box groove, removable templates, and telescopic bolt shanks. The latter two moved together to form a tightly connected sample space. The template could be removed; therefore, the intact specimen was easy to remove from the device.

## 3. Materials and Methods

**3.1. Materials.** The investigation was carried out on loess with an original water content of  $18 \pm 4\%$ , which is widely distributed on the surface of mining area in Shaanxi area of West China. The properties of the prepared soil samples are shown in Table 1, and their particle-size distribution curves are shown in Figure 3. The parameters for evaluating the soil particle gradation are  $c_u = 3.07$  and  $c_c = 0.94$ . The soils can be considered well-graded soils. The collected loess was air dried, crushed (so as not to destroy the natural structure), and sieved at 2 mm in the laboratory before the test.

**3.2. Procedures.** A total of 1 kg of the sifted soil were put in a plastic barrel, and water was added with a small spray bottle until the desired water content was reached. The barrel was sealed, and soil was left for at least 3 days to homogenize. Subsequently, the soils were compacted layer by layer (a total of three equal layers) to the required dry density in a homemade mold. Vaseline was applied to the inner wall to ensure that the sample could be completely removed. Samples were prepared at water contents of 14, 16, 18, and 20% and compacted to 1.55 and 1.65 g/cm<sup>3</sup>.

Each sample was installed in the tensile apparatus and covered with a thin layer of Vaseline to prevent evaporation. To evaluate the mechanical behavior of the material, two kinds of tests were performed: (i) direct tensile tests at different water contents and (ii) loading-unloading cyclic tests while maintaining or increasing the maximum load per cycle. All of the unloading levels were higher than the yield limit. The uniaxial stress  $\sigma$  and strain  $\varepsilon$  can be denoted by the theory of solid mechanics:

$$\begin{aligned}\sigma &= \frac{F}{A_0}, \\ \varepsilon &= \frac{\Delta L}{L_0},\end{aligned}\quad (1)$$

where  $F$  is the axial force,  $A_0$  is the cross-sectional area,  $\Delta L$  is the elongation at the corresponding tensile force  $F$ , and  $L_0$  is the effective length. The effective length  $L_0$  is calculated as the sample length minus the length between the two clamps. In this study,  $L_0 = 60$  mm and  $A_0 = 30 \times 30$  mm.

## 4. Results and Discussion

**4.1. Direct Tensile Tests.** Direct tensile tests were performed on three identical samples. The mean mechanical parameters (i.e., elastic modulus, yield limit, tensile strength, and ultimate strain) obtained experimentally are presented in Table 2.

The measurement of the elastic modulus and yield limit presents experimental problems depending on soil type, state, constitutive relations, and test precision. In this study, the elastic modulus was obtained using the following method. The stress-strain curve was initially approximately a straight line (regarded as the elastic phase) and gradually showed nonlinearity with increasing axial load. The following equation was employed to describe this behavior [23]:

$$\sigma = \sigma_t \left[ 1 - \left( 1 - \frac{\varepsilon}{\varepsilon_t} \right)^A \right], \quad (2)$$

where  $\sigma_t$  is the tensile strength,  $\varepsilon_t$  is the ultimate failure strain, and  $A$  is the fitting modulus. The stress-strain data and fitting curves of one sample are shown in Figure 4. The elastic modulus can be calculated:

$$E_0 = \frac{d\sigma}{d\varepsilon} \Big|_{\varepsilon=0} = \frac{A \cdot \sigma_t}{\varepsilon_t}. \quad (3)$$

Plastic deformation will occur when the stress exceeds the yield strength. So the yield limit  $\sigma_0$  is exactly the initial stress of plastic deformation. Plastic deformation can be obtained

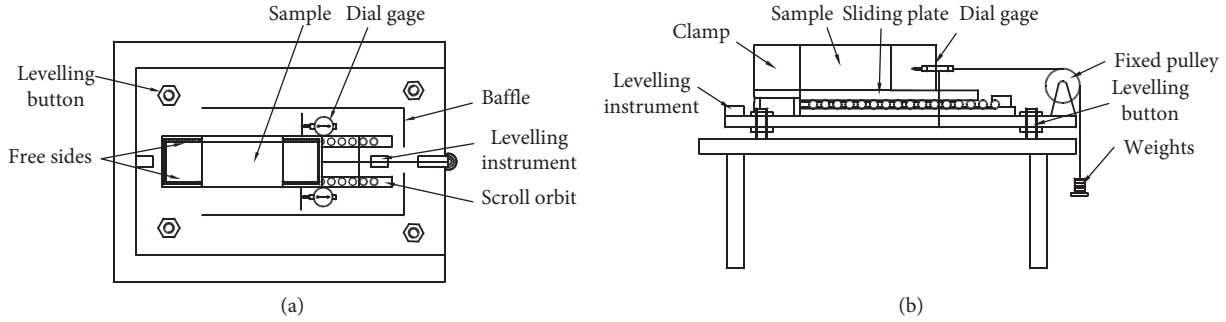


FIGURE 1: Schematic drawing of the tension apparatus: (a) vertical view; (b) side view.

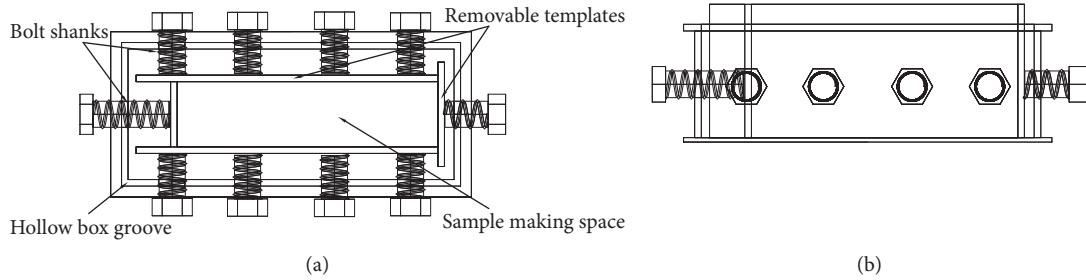


FIGURE 2: Schematic drawing of the compaction apparatus: (a) vertical view; (b) side view.

TABLE 1: Physical properties of the compacted soils.

Specific gravity (gs)	Plastic limit, PL (%)	Liquid limit, LL (%)	Plasticity index, PI (%)	Maximum dry density, $\rho_{d\max}$ (g/cm <sup>3</sup> )	Optimum water content, $\omega_{opt}$ (%)
2.65	17.4	26.0	8.6	1.76	16.2

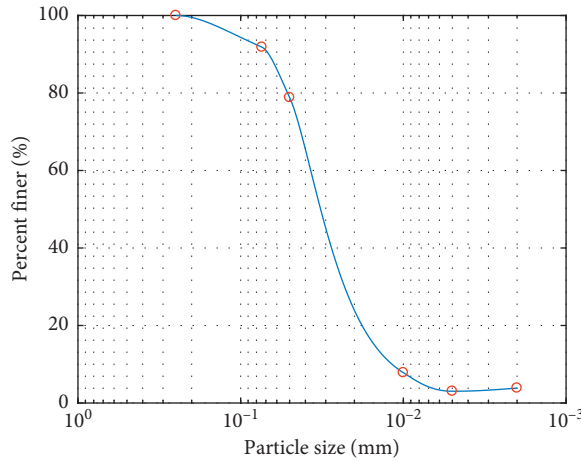


FIGURE 3: Particle-size distribution curve of the test materials.

TABLE 2: Mechanical properties of the remolded loess.

Properties	$\rho_d = 1.55 \text{ g/cm}^3$				$\rho_d = 1.65 \text{ g/cm}^3$			
	$\omega = 14\%$	$\omega = 16\%$	$\omega = 18\%$	$\omega = 20\%$	$\omega = 14\%$	$\omega = 16\%$	$\omega = 18\%$	$\omega = 20\%$
Elastic modulus, $E_0$ (MPa)	25.7	18.9	15.1	7.0	28.3	25.0	19.7	9.7
Yield limit, $\sigma_0$ (kPa)	14	10	8	6	20	14	10	8
Tensile strength, $\sigma_t$ (kPa)	35.4	26.5	20.7	15.3	41	37.5	23.3	18.2
Ultimate strain, $\varepsilon_t$ (%)	0.20	0.25	0.30	0.40	0.22	0.28	0.35	0.48

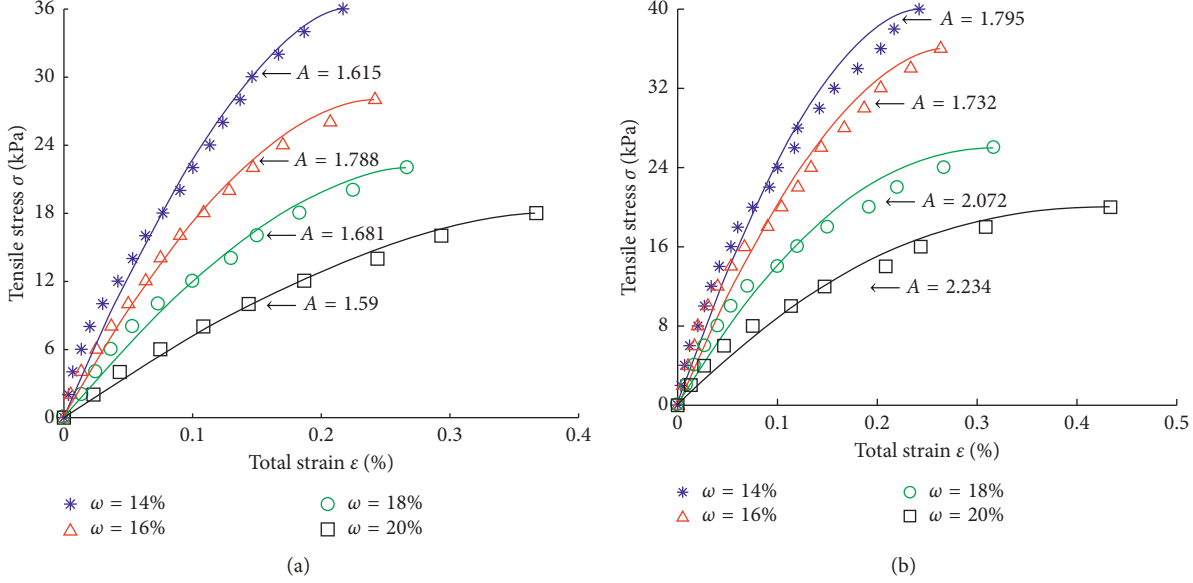


FIGURE 4: Direct tensile test  $\sigma \times \varepsilon$  curves at different water contents: (a)  $\rho_d = 1.55 \text{ g/cm}^3$ ; (b)  $\rho_d = 1.65 \text{ g/cm}^3$ .

according to elastic-plastic mechanics, which can be obtained by the following equation:

$$\begin{aligned}\varepsilon &= \varepsilon^e + \varepsilon^p, \\ \varepsilon^e &= \frac{\sigma}{E_0}, \\ \varepsilon^p &= \varepsilon - \frac{\sigma}{E_0} \geq 0,\end{aligned}\quad (4)$$

where  $\varepsilon^e$  is the elastic strain,  $\varepsilon^p$  is the plastic strain, and yield limit  $\sigma_0$  is the minimum stress value in upper formula (i.e.  $\sigma_0 = \sigma \leq \varepsilon \cdot E_0|_{\sigma=\sigma_{\min}}$ ).

Both the yield limit and elastic modulus decreased with increasing water content. The tensile strength also decreased with increasing water content over a certain range [11, 18, 24, 25]. The yield limit and elastic modulus in the tests were strongly correlated with the tensile strength (Figure 5). The yield limit and elastic modulus can be expressed by linear functions:

$$\begin{aligned}\sigma_0 &= \alpha \sigma_t + m p_a, \\ E_0 &= \beta \sigma_t + n p_a,\end{aligned}\quad (5)$$

where  $p_a$  is the atmospheric pressure, which was used to convert the vertical and horizontal coordinates into dimensionless quantities;  $\alpha$  and  $\beta$  are the modulus numbers; and  $m$  and  $n$  are constants; the values of  $\alpha$ ,  $\beta$ ,  $m$ , and  $n$  can be determined from the test results.

Figure 4 shows that the strain continued to increase with tensile stress until fracturing occurred. What we are interested in is how the plastic strain changes when the stress exceeds the yield limit, that is, plastic constitutive relation under direct tension. Stress can be assumed as a function of total plastic work  $W_p$  from the standpoint of energy mechanism [26]. In a limited deformation process,  $W_p$  is defined as the work consumed by plastic deformation per unit

volume (i.e., plastic specific work). Based on the assumption, the plastic constitutive relation of this material can be written as

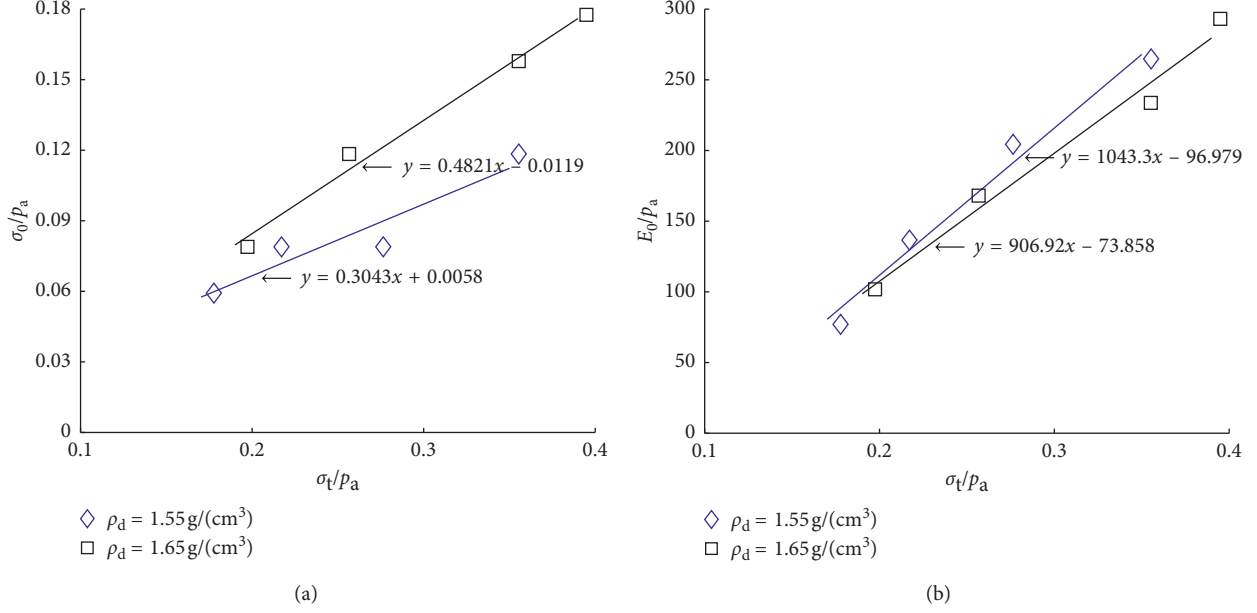
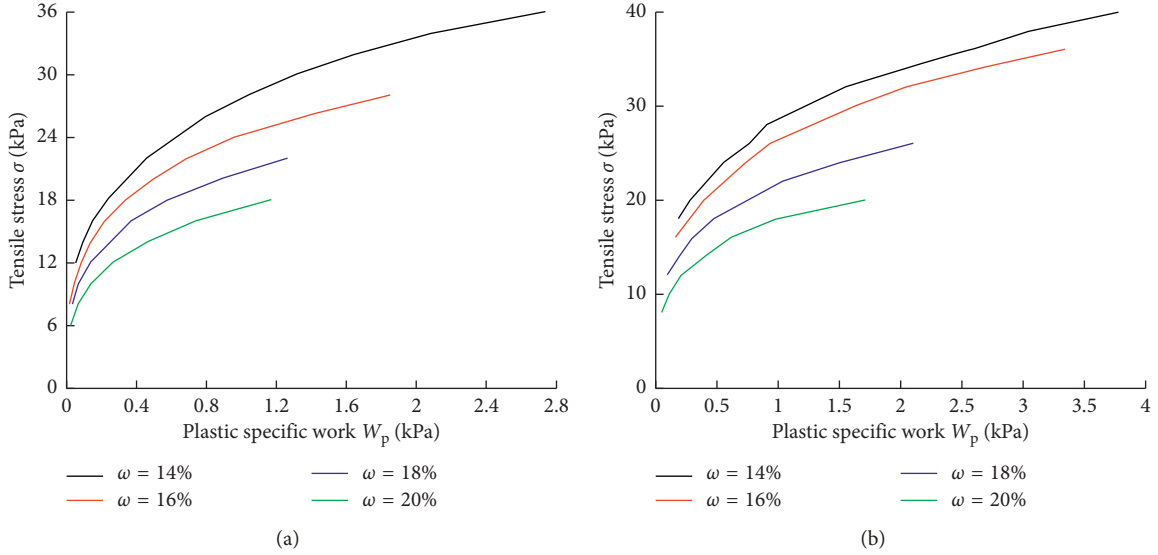
$$\sigma = F(W_p). \quad (6)$$

In uniaxial tensile testing, the plastic specific work can be expressed as follows:

$$W_p = \int \sigma d\varepsilon^p = \int \sigma \left( \frac{dl}{l} - \frac{d\sigma}{E_0} \right) = \int_{l_0}^l \frac{\sigma dl}{l} - \frac{\sigma^2}{2E_0}, \quad (7)$$

where  $dl/l$  is the total strain increment,  $d\sigma/E_0$  is the elastic strain increment,  $l$  is the instantaneous length of the sample,  $l_0$  is the initial length of the sample ( $l_0 = L_0 = 60 \text{ mm}$ ), and the difference between  $dl/l$  and  $d\sigma/E_0$  ( $dl/l - d\sigma/E_0$ ) is the plastic strain increment. The stress  $\sigma$  is greater than the yield stress  $\sigma_0$  ( $\sigma > \sigma_0$ ). In Figure 6, it could be intuitively seen that the plastic work was zero at low stress level. When the stress exceeded the yield limit, the growth rate of plastic specific work was getting faster and faster. In addition, under the same stress condition, the plastic work consumed by the sample with high moisture content was obviously higher than that of the sample with low moisture content. It was illustrated that water content was a key factor affecting plastic deformation, and the higher the moisture content was, the more significant the plastic deformation would be. Plastic constitutive equation could also be described by another way  $\sigma = \varphi(\varepsilon^p)$ . The results are shown in Figure 7. Obviously, the plasticity development was consistent with Figure 6.

**4.2. Cyclic Loading-Unloading Tests.** In order to further study the elastoplastic characteristics, particularly the plastic deformation, loading-unloading cyclic tests were carried out at room temperature. The dry density was  $1.55 \text{ g/cm}^3$ , and the water contents were 16% and 18%. The loading histories are shown in Table 3.

FIGURE 5: Relationships of the tensile strength with (a) yield limit  $\sigma_0$  and (b) elastic modulus  $E_0$ .FIGURE 6: Plastic constitutive relation  $\sigma = F(W_p)$  with (a)  $\rho_d = 1.55 \text{ g/cm}^3$  and (b)  $\rho_d = 1.65 \text{ g/cm}^3$ .

**4.2.1. Stress-Strain Analysis.** The stress-strain curves for loading patterns I and II are shown (only the data of cyclic loading and unloading are presented) in Figures 8 and 9, respectively. The loading and unloading gradients were the same (2 kPa) to minimize interfering factors.

Hysteresis loops were produced under each loading and unloading cycle, which led to dissipation of mechanical energy. Similar trends were reported in [27]. Each loading curve was fitted by linear function, and the results are shown in Table 4. It could be seen that the fitted slopes of the loading curves decreased gradually, which quantitatively indicated that the elastic modulus decreased with the cyclic loading.

After a cycle of loading and unloading, the distance between the soil particles may increase, so the original dry density of the sample would decrease with it. Thus, the connecting force and adhesion may be weakened, which may reduce the ability of the soil to resist deformation (i.e., stiffness). The tensile deformation of the specimen increases gradually, and no “ultimate compaction deformation” was identified in the tests.

The deformation after a loading-unloading cycle increased due to the stress history. In Figure 10, points A and B have the same stress  $\sigma$ , but they correspond to different strains  $\epsilon$ . Point A is on the initial loading curve, and point B is on the reloading curve. The strain increment  $\Delta\epsilon^B$  is larger

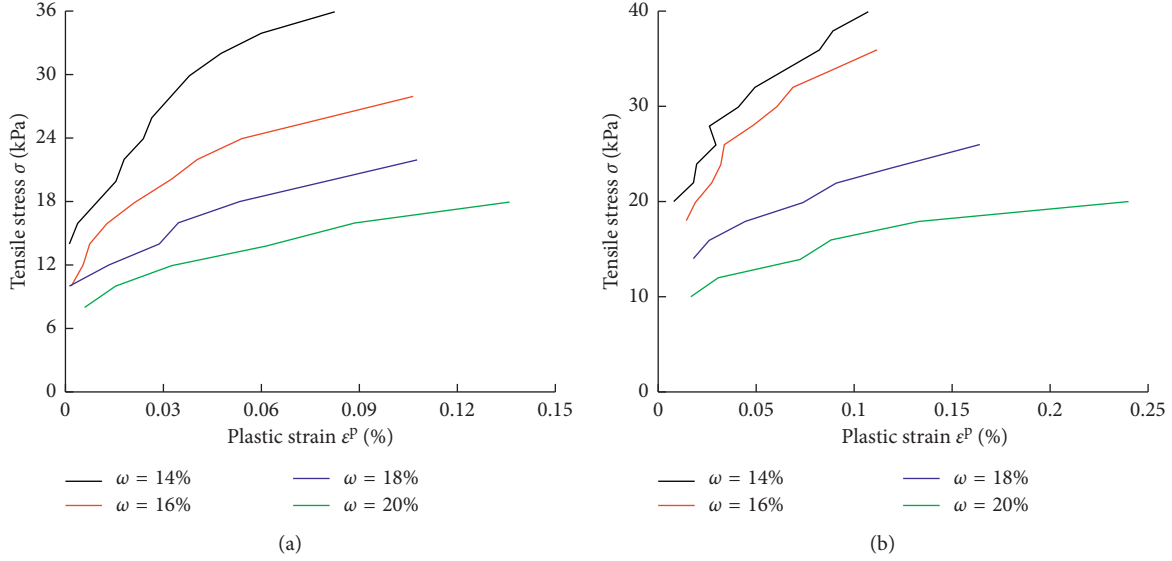


FIGURE 7: Plastic constitutive relation  $\sigma = \varphi(\varepsilon^P)$  with (a)  $\rho_d = 1.55 \text{ g/cm}^3$  and (b)  $\rho_d = 1.65 \text{ g/cm}^3$ .

TABLE 3: Loading histories.

Sample type	Loading pattern	Maximum loading stress (kPa)	Minimum unloading stress (kPa)
$\rho_d = 1.55 \text{ g/cm}^3, \omega = 16\%$	I	20	0
	II	16 → 18 → 20 → 22...	0
$\rho_d = 1.55 \text{ g/cm}^3, \omega = 18\%$	I	16	0
	II	12 → 14 → 16 → 18...	0

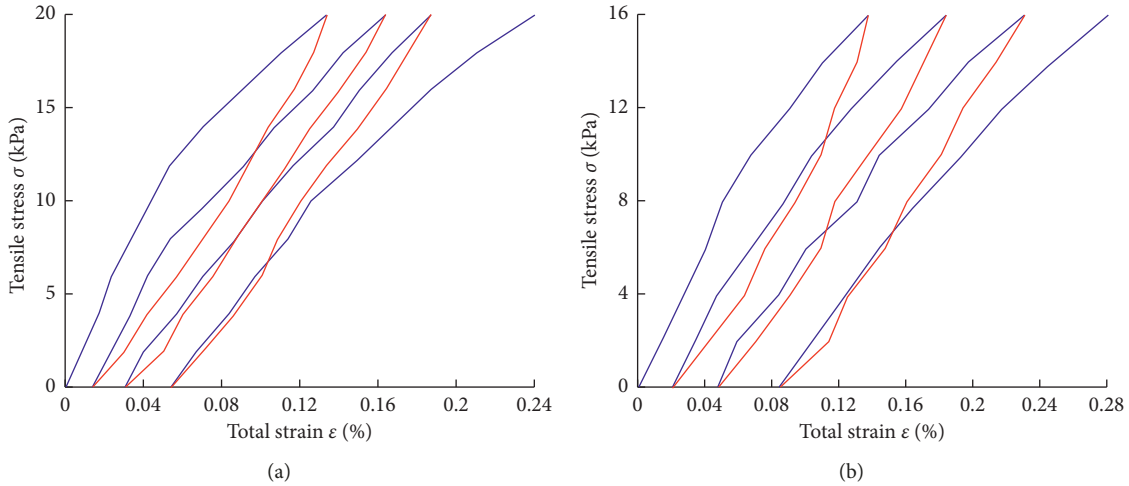


FIGURE 8: Stress-strain curves of the cyclic tensile tests for loading pattern I: (a)  $w = 16\%$ ; (b)  $w = 18\%$ .

than  $\Delta\varepsilon^A$  for the same load increment  $\sigma$  because A and B have different stress histories. In conventional cyclic loading tests including uniaxial and triaxial compression, soil compression can increase the soil density, reduce the pore space, and force air and/or water from the pores [28, 29]. However, there are no restrictions to deformation in direction of axial tension, so no strain limit was observed.

The cyclic stress-plastic strain curves are shown in Figures 11 and 12. Similarly, the plastic deformation exhibited hysteresis (a phase lag), which showed that the

plastic deformation recovered slightly. During unloading, in theory, plastic strain should have been constant, and the total deformation (elastic and plastic deformation) recovered due to the recovery of elastic strain. In this test, the decrease of plastic deformation may be caused by the inertia of the elastic recovery. Plastic strain would decrease slightly with the elastic recovery.

In addition, the tensile strengths of the samples decreased compared with the direct tests by varying degrees (Figure 13). The stiffness of the specimen decreased after the cyclic loading,

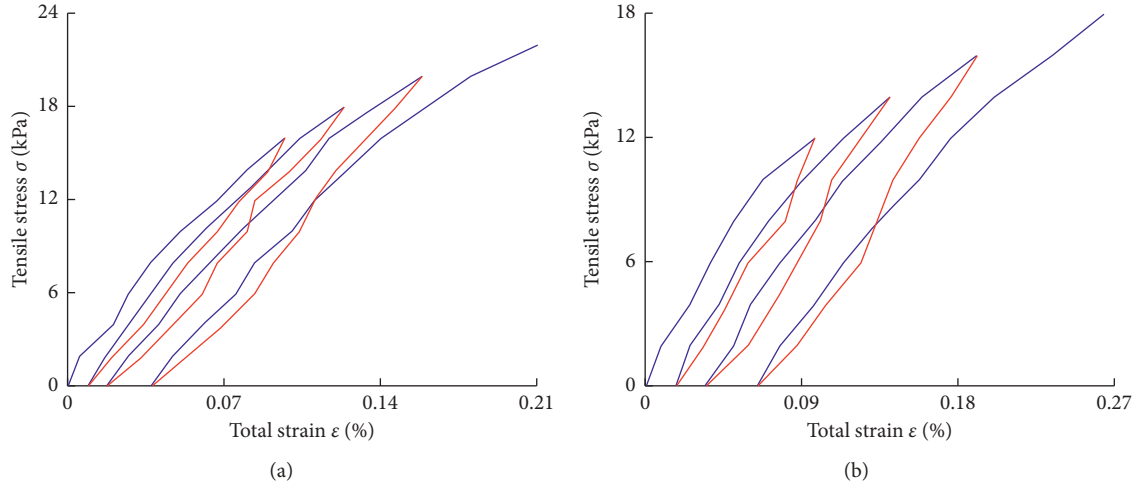


FIGURE 9: Stress-strain curves of the cyclic tensile tests for loading pattern II: (a)  $w = 16\%$ ; (b)  $w = 18\%$ .

TABLE 4: Fitting slopes of the loading curves ( $\sigma \times \varepsilon$ ).

Water content		Linear fitting of loading curves			
		1st	2nd	3rd	4th
Pattern I	16%	$y = 149.29x + 2.1058$	$y = 129.5x - 0.2223$	$y = 126.58x - 3.1179$	$y = 109.03x - 4.7518$
	18%	$y = 118.52x + 0.9766$	$y = 97.668x - 0.8987$	$y = 86.676x - 3.1876$	$y = 81.932x - 6.1712$
Pattern II	18%	$y = 162.14x + 1.124$	$y = 155.99x - 0.1516$	$y = 143.52x - 1.5248$	$y = 131.5x - 3.538$
	16%	$y = 125.86x + 0.9057$	$y = 111.83x - 0.6882$	$y = 103.32x - 2.504$	$y = 89.867x - 4.5849$

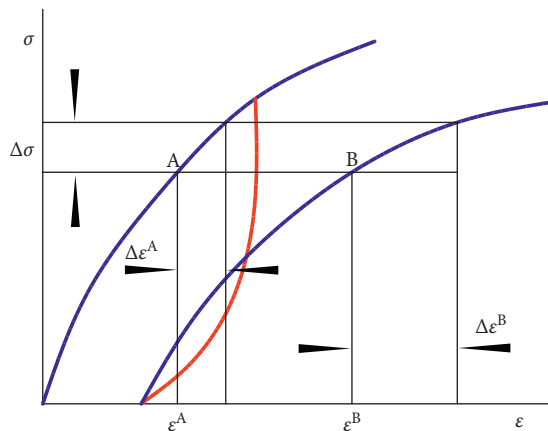


FIGURE 10: Influence of the stress history on deformation.

which may also have led to weakening of the interparticle connection and cohesion force. The cyclic loading caused the repeated growth of microcracks in the material, which finally resulted in the deterioration of the mechanical properties. Therefore, even though the cyclic force was less than the tensile strength, macroscopic cracks would be slowly produced by the accumulation of fatigue damage. There was no doubt that this would lead to the specimen fracture.

#### 4.2.2. Mathematical Model of Cyclic Loading Curves.

Section 4.2.1 showed that loading patterns I and II (including strain and plastic strain) had the same pattern. Based on the results shown in Figures 8, 9, 11, and 12, the ideal de-

formation curves of loading pattern I (including strain and plastic strain) are assumed in Figure 14. Pattern II is omitted as it is similar to pattern I.

Each loading curve of the cyclic strain or plastic strain (Figure 14) could be divided into two stages (i.e., before and after the yield stress), which were represented by the blue and black segments, respectively. In Figure 14(a), the following functions can describe the relationship between the loading stress and strain:

$$\sigma = E \cdot \varepsilon, \quad \sigma \leq \sigma_0, \quad (8)$$

$$\sigma = \Phi(\varepsilon), \quad \sigma > \sigma_0, \quad (9)$$

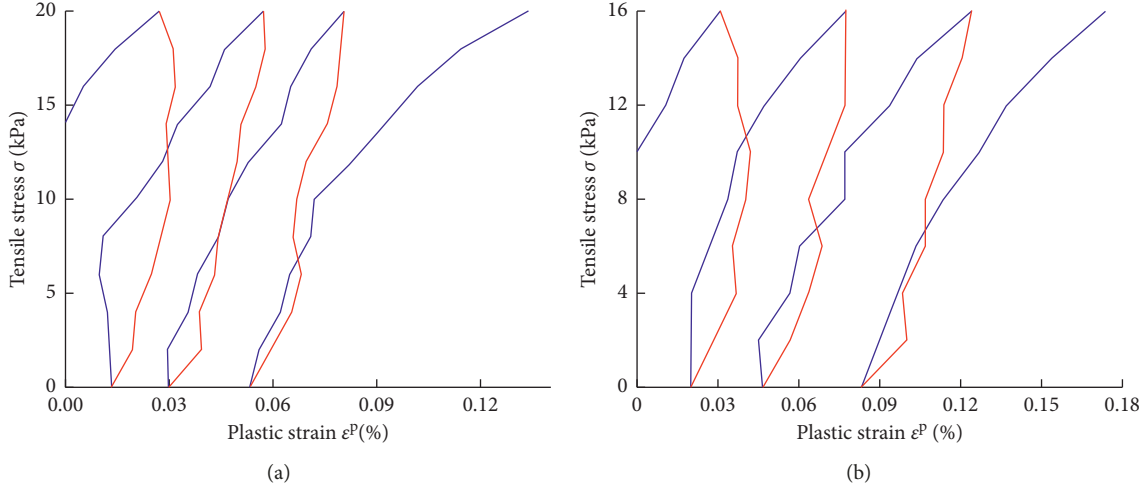


FIGURE 11: Stress-plastic strain curves of the cyclic tensile tests for load pattern I: (a)  $w = 16\%$ ; (b)  $w = 18\%$ .

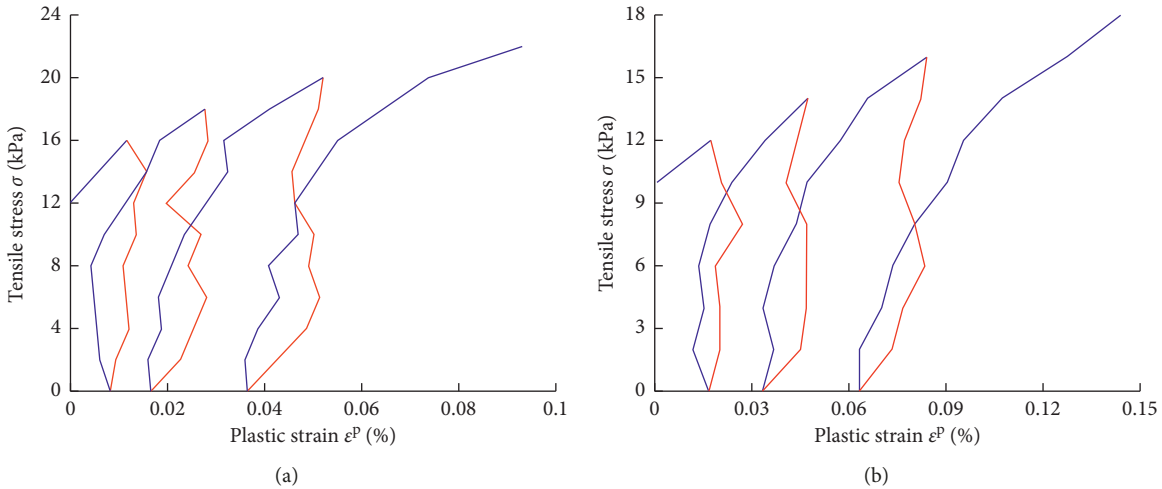


FIGURE 12: Stress-plastic strain curves of the cyclic tensile tests for load pattern II: (a)  $w = 16\%$ ; (b)  $w = 18\%$ .

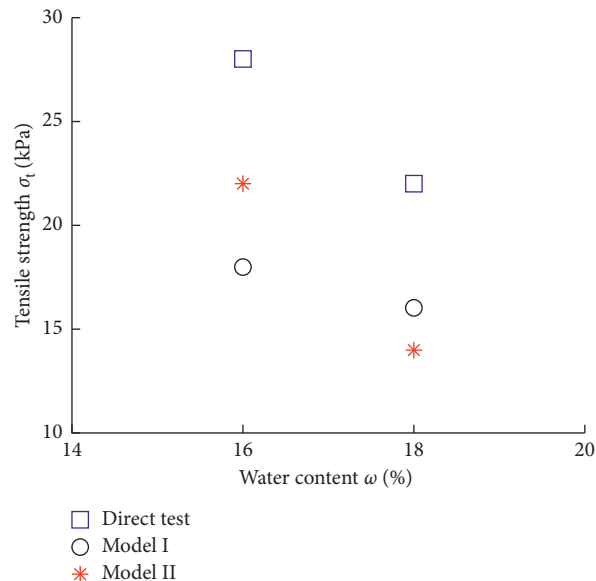


FIGURE 13: Variation in the tensile strength with cyclic loading.

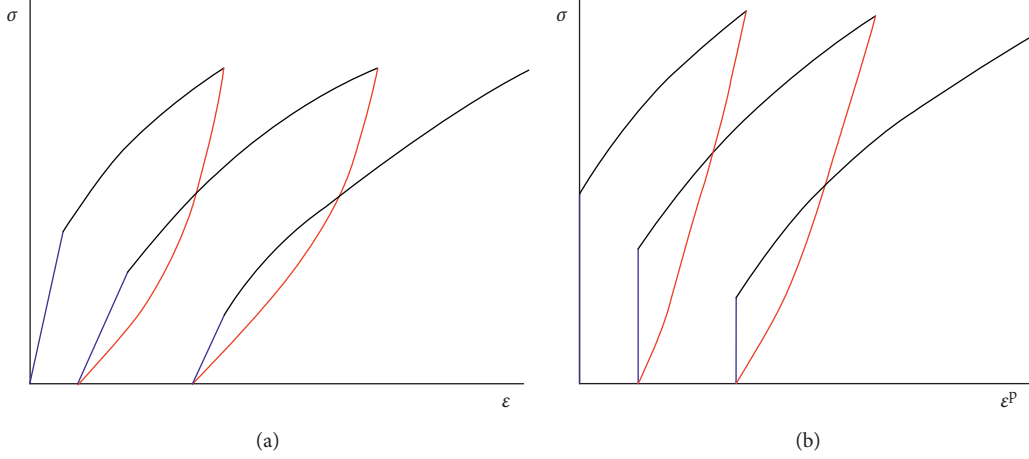
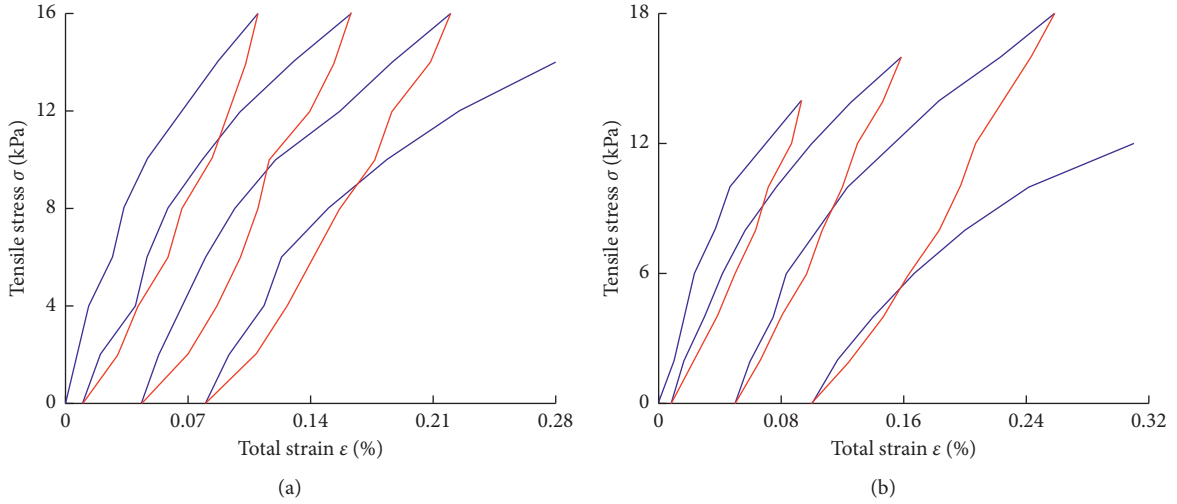
FIGURE 14: Deformation models under cyclic loading with (a)  $\sigma \times \varepsilon$  curve and (b)  $\sigma \times \varepsilon^P$  curve.

FIGURE 15: Stress-strain curves of the cyclic tests for (a) loading pattern I and (b) loading pattern II.

TABLE 5: Calculated yield limits.

Specimen	Yield limit			
	Loading order			
	1st	2nd	3rd	4th
$\rho_d = 1.65 \text{ g/cm}^3, \omega = 18\%$				
Pattern I	12	10	10	8
Pattern II	12	10	8	4

where  $E$  is the slope of first straight line, which decreases with the number of cycles. The second is curvilinear because of the plastic deformation.

In Figure 14(b), the loading curves can be expressed by

$$\begin{aligned} \varepsilon^P &= n, & \sigma \leq \sigma_0, \\ \varepsilon^P &= \varepsilon - \frac{\Phi(\varepsilon)}{E}, & \sigma > \sigma_0. \end{aligned} \quad (10)$$

In first curve,  $n$  is a constant. In second curve, plastic strain  $\varepsilon^P$  is a function of strain  $\varepsilon$ , but we prefer to obtain the

relationship between stress  $\sigma$  and plastic strain  $\varepsilon^P$  in order to be more intuitive. The function can be got from formula (9):

$$\varepsilon^P = \Phi^{-1}(\sigma), \quad \sigma > \sigma_0. \quad (11)$$

Furthermore, the phenomenological model of describing cyclic plastic strain is given by

$$\varepsilon^P = \varepsilon_0^P = \varepsilon_0 = n, \quad \sigma \leq \sigma_0, \quad (12)$$

$$\sigma = f^{-1}(\varepsilon^P) = f^{-1}\left(\Phi^{-1}(\sigma) - \frac{\sigma}{E}\right), \quad \sigma > \sigma_0, \quad (13)$$

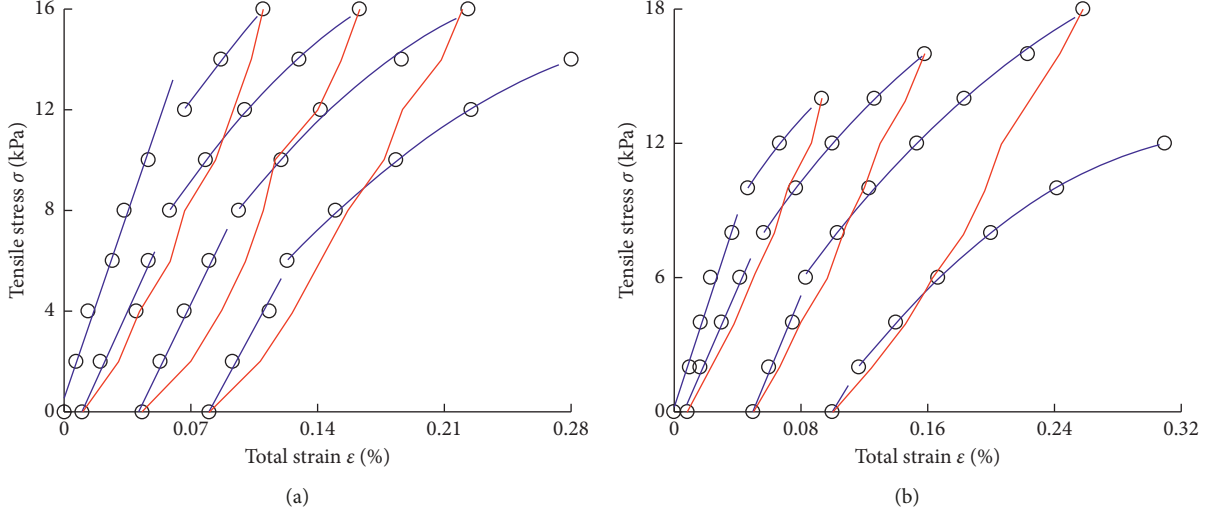


FIGURE 16: Function fitting of the stress-strain curves for (a) loading pattern I and (b) loading pattern II.

TABLE 6: Model parameters from the best-fitting stress-strain curves.

	Loading curves											
	1st			2nd			3rd			4th		
	$E$ (MPa)	$a$	$b$	$c$	$E$ (MPa)	$a$	$b$	$c$	$E$ (MPa)	$a$	$b$	$c$
Pattern I	21.1	-180	123	5	15.9	-276	137	1	149	-221	132	-3
Pattern II	21.6	-532	160	4	16.3	-232	128	2	17.2	-160	121	-3
		13.1	-155	1135								
		-185	1305	-11								

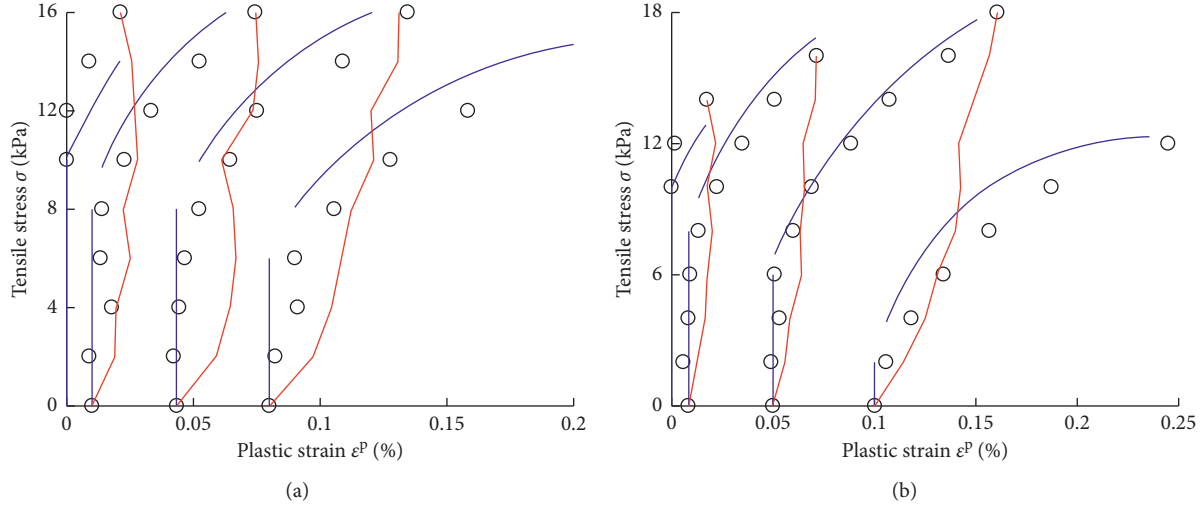


FIGURE 17: The comparisons of measured data and fitted functions by proposed model for (a) loading pattern I and (b) loading pattern II.

where  $\varepsilon_0^P$  and  $\varepsilon_0$  are, respectively, the plastic strain and strain after unloading and  $\Phi^{-1}(\sigma)$  and  $f^{-1}(\varepsilon^P)$  are the inverse functions of  $\Phi(\varepsilon)$  and  $f(\sigma)$ , respectively.

So, to sum up, the proposed mathematical model (equations (12) and (13)) can be used to predict plastic deformation by the initial loading stress-strain curves ( $\sigma \times \varepsilon$ ). Next, it would be validated with new data. The stress-strain curves of samples of  $w = 18\%$  and  $\rho_d = 1.65 \text{ g/cm}^3$  are shown in Figure 15. The obtained yield limits are listed in Table 5.

In Figure 15, the second curve is assumed as a quadratic function. Therefore, equation (9) can be written as

$$\sigma = \Phi(\varepsilon) = a\varepsilon^2 + b\varepsilon + c, \quad \sigma > \sigma_0, \quad (14)$$

where  $a$ ,  $b$ , and  $c$  are parameters. The resulting curves for cyclic stress-strain are shown as blue curves in Figure 16, and the best fit  $a$ ,  $b$ ,  $c$ , and  $E$  values are presented in Table 6.

Then, the cyclic plastic strain are obtained using the expressions in equations (12)–(14). The measured tensile

stress-plastic strain curves are fitted using the proposed mathematical model (shown in Figure 17).

The fitted curves reproduced the test results well, which demonstrated that the proposed mathematical model could reasonably represent the tensile plasticity characteristics of compacted soils under cyclic loading tension. The model combined enough mathematical simplicity, and it could describe a nonlinear mechanical behaviour of plastic deformation observed in cyclic tests. In addition, in this paper, the expression of yield strength  $\sigma_0$  in cyclic loading was not obtained, which would be a direction of effort in the future. An analysis of plastic strain of unloading curves was beyond the scope of this study. More comprehensive experimental and theoretical studies should be conducted to address the idealizations and assumptions used in the models. Much work remained to accurately describe and predict plastic deformation of compacted soils under cyclic loading.

## 5. Conclusions

Almost all the data were recorded instantaneously in the experimental investigation, and there was no effect of creep on deformation. The effect of time or viscosity on deformation had been ignored. Consequently, the behavior is approximately considered elastic-plastic, rather than elastic-viscoplastic or viscoelastic. The stress-strain (mainly plastic strain) characteristics under direct and cyclic loading were studied in this paper. The following conclusions were drawn. For the direct test, the yield limit, elastic modulus, and tensile strength had the same trends with the water content.  $\sigma = F(W_p)$  and  $\sigma = \varphi(\varepsilon^p)$  were two methods to describe plastic constitutive relation, and both presented the same rule. For cyclic loading-unloading test, the material exhibited hysteresis. The stiffness of remolded loess gradually decreased. And importantly, there was no compaction limit observed with the cycle numbers. The plastic deformation of cyclic loading curves was analyzed. The plastic deformation hysteresis loop may be caused by elastic shrinkage. The fatigue failure may occur with the progressive accumulation of plastic strain. In the end, an elastic-plastic phenomenological model was proposed, which could describe the plastic cyclic behaviour. The model was mathematically simple enough to be used for plastic strain predictions in cyclic tests.

## Data Availability

The data used to support the findings of this study are included within the article.

## Conflicts of Interest

The authors declare that they have no conflicts of interest.

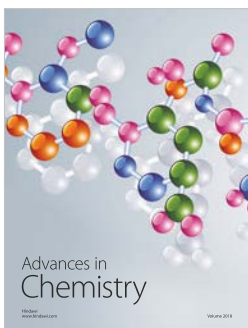
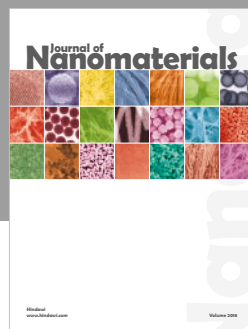
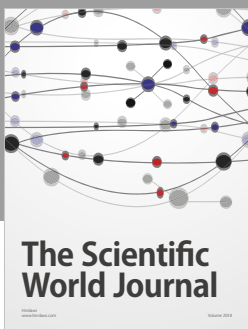
## Acknowledgments

This work was supported by Outstanding Innovation Scholarship for Doctoral Candidate of “Double First Class” Construction Disciplines of CUMT.

## References

- [1] A. Groisman and E. Kaplan, “An experimental study of cracking induced by desiccation,” *Europhysics Letters (EPL)*, vol. 25, no. 6, pp. 415–420, 1994.
- [2] H. Peron, L. Hueckel, L. Laloui, and L. B. Hu, “Fundamentals of desiccation cracking of fine-grained soils: experimental characterisation and mechanisms identification,” *Canadian Geotechnical Journal*, vol. 46, no. 10, pp. 1175–1201, 2009.
- [3] J.-M. Konrad and R. Ayad, “A idealized framework for the analysis of cohesive soils undergoing desiccation,” *Canadian Geotechnical Journal*, vol. 34, no. 4, pp. 477–488, 1997.
- [4] C.-S. Tang, X.-J. Pei, D.-Y. Wang, B. Shi, and J. Li, “Tensile strength of compacted clayey soil,” *Journal of Geotechnical and Geoenvironmental Engineering*, vol. 141, no. 4, Article ID 04014122, 2015.
- [5] H. Nahlawi and J. K. Kodikara, “Laboratory experiments on desiccation cracking of thin soil layers,” *Geotechnical and Geological Engineering*, vol. 24, no. 6, pp. 1641–1664, 2006.
- [6] P. H. Morris, J. Graham, and D. J. Williams, “Cracking in drying soils,” *Canadian Geotechnical Journal*, vol. 29, no. 2, pp. 263–277, 1992.
- [7] B. A. Albrecht and C. H. Benson, “Effect of desiccation on compacted natural clays,” *Journal of Geotechnical and Geo-environmental Engineering*, vol. 127, no. 1, pp. 67–75, 2001.
- [8] E. Alonso, S. Olivella, and D. Arnedo, “Mechanisms of gas transport in clay barriers,” *Journal of Iberian Geology*, vol. 32, pp. 175–196, 2006.
- [9] S. Olivella and E. E. Alonso, “Gas flow through clay barriers,” *Géotechnique*, vol. 58, no. 3, pp. 157–176, 2008.
- [10] P. D. Hallett, A. R. Dexter, and J. P. K. Seville, “The application of fracture mechanics to crack propagation in dry soil,” *European Journal of Soil Science*, vol. 46, no. 4, pp. 591–599, 1995.
- [11] S. Y. Ibarra, E. McKyes, and R. S. Broughton, “Measurement of tensile strength of unsaturated sandy loam soil,” *Soil and Tillage Research*, vol. 81, no. 1, pp. 15–23, 2005.
- [12] T. H. Kim, C. K. Kim, S. J. Jung, and J. H. Lee, “Tensile strength characteristics of contaminated and compacted sand-bentonite mixtures,” *Environmental Geology*, vol. 52, no. 4, pp. 653–661, 2007.
- [13] P. V. Divya, B. V. S. Viswanadham, and J. P. Gourc, “Evaluation of tensile strength-strain characteristics of fiber-reinforced soil through laboratory tests,” *Journal of Materials in Civil Engineering*, vol. 26, no. 1, pp. 14–23, 2014.
- [14] R. N. Tollenaar, L. A. van Paassen, and C. Jommi, “Experimental evaluation of the effects of pull rate on the tensile behavior of a clay,” *Applied Clay Science*, vol. 144, pp. 131–140, 2017.
- [15] T.-H. Kim and C. Hwang, “Modeling of tensile strength on moist granular earth material at low water content,” *Engineering Geology*, vol. 69, no. 3-4, pp. 233–244, 2003.
- [16] N. Lu and W. J. Likos, “Suction stress characteristic curve for unsaturated soil,” *Journal of Geotechnical and Geo-environmental Engineering*, vol. 132, no. 2, pp. 131–142, 2006.
- [17] N. Lu, B. Wu, and C. P. Tan, “Tensile strength characteristics of unsaturated sands,” *Journal of Geotechnical and Geo-environmental Engineering*, vol. 133, no. 2, pp. 144–154, 2007.
- [18] H. Trabelsi, M. Jamei, H. Zenzri, and S. Olivella, “Crack patterns in clayey soils: experiments and modeling,” *International Journal for Numerical and Analytical Methods in Geomechanics*, vol. 36, no. 11, pp. 1410–1433, 2012.
- [19] D. S. Liu and A. S. An, “Loess from China,” *Acta Geologica Sinica*, vol. 42, pp. 1–18, 1962.

- [20] L. Xu and M. R. Coop, "Influence of structure on the behavior of a saturated clayey loess," *Canadian Geotechnical Journal*, vol. 53, no. 6, pp. 1026–1037, 2016.
- [21] Y. Li, "A review of shear and tensile strengths of the Malan Loess in China," *Engineering Geology*, vol. 236, pp. 4–10, 2018.
- [22] S. He, H. Bai, and Z. Xu, "Evaluation on tensile behavior characteristics of undisturbed loess," *Energies*, vol. 11, pp. 1–18, 2018.
- [23] V. S. Gopalaratnam and P. S. Surendra, "Softening response of plain concrete in direct tension," *ACI Journal Proceedings*, vol. 82, no. 3, pp. 310–323, 1985.
- [24] G. D. Towner, "The tensile stress generated in clay through drying," *Journal of Agricultural Engineering Research*, vol. 37, no. 3-4, pp. 279–289, 1987.
- [25] P. Sun, J.-B. Peng, L.-W. Chen, Y.-P. Yin, and S.-R. Wu, "Weak tensile characteristics of loess in China—an important reason for ground fissures," *Engineering Geology*, vol. 108, no. 1-2, pp. 153–159, 2009.
- [26] W. Prage and P. G. Hodgo, *Theory of Perfectly Plastic Solids*, New York Press, New York, NY, USA, 1951.
- [27] B.-Y. Zhang, Q.-M. Li, H.-N. Yuan, and X. Sun, "Tensile fracture characteristics of compacted soils under uniaxial tension," *Journal of Materials in Civil Engineering*, vol. 27, no. 10, Article ID 04014274, 2015.
- [28] R. Horn and M. Lebert, "Soil compactability and compressibility," *Developments in Agricultural Engineering*, vol. 11, pp. 45–69, 1994.
- [29] P. I. Gubiani, P. Pértle, and J. M. Reichert, "Relationship of precompression stress with elasticity and plasticity indexes from uniaxial cyclic loading test," *Soil and Tillage Research*, vol. 180, pp. 29–37, 2018.



Hindawi

Submit your manuscripts at  
[www.hindawi.com](http://www.hindawi.com)

